



HAL
open science

An All-Digital Optical Phase-Locked Loop Suitable for Satellite Downlinks

Jognes Panasiewicz, Nisrine Arab, Fabien Destic, Gefeson M. Pacheco,
Angélique Rissons

► **To cite this version:**

Jognes Panasiewicz, Nisrine Arab, Fabien Destic, Gefeson M. Pacheco, Angélique Rissons. An All-Digital Optical Phase-Locked Loop Suitable for Satellite Downlinks. *Photonics*, 2023, 10 (12), pp.1312-10.3390/photonics10121312 . hal-04337024

HAL Id: hal-04337024

<https://hal.science/hal-04337024>




Submitted on 12 Dec 2023

HAL is a multi-disciplinary open access archive for the deposit and dissemination of scientific research documents, whether they are published or not. The documents may come from teaching and research institutions in France or abroad, or from public or private research centers.

L'archive ouverte pluridisciplinaire **HAL**, est destinée au dépôt et à la diffusion de documents scientifiques de niveau recherche, publiés ou non, émanant des établissements d'enseignement et de recherche français ou étrangers, des laboratoires publics ou privés.

Article

An All-Digital Optical Phase-Locked Loop Suitable for Satellite Downlinks [†]

Jognes Panasiewicz ^{1,*}, Nisrine Arab ², Fabien Destic ², Gefeson M. Pacheco ³ and Angélique Rissons ²¹ Instituto Nacional de Pesquisas Espaciais (INPE), São José dos Campos 12227-010, Brazil² ISAE-Supaero, Université de Toulouse, 31400 Toulouse, France; arabnisrine91@gmail.com (N.A.); fabien.destic@isae-superaero.fr (F.D.); angelique.rissons@isae-superaero.fr (A.R.)³ Instituto Tecnológico de Aeronáutica (ITA), São José dos Campos 12228-900, Brazil; gpacheco@ita.br

* Correspondence: jognes.panasiewicz@inpe.br

[†] This paper is an extend version of our paper: J. Panasiewicz, N. Arab, F. Destic, G.M. Pacheco and A. Rissons, All-Digital Optical Phase-Locked Loop for Satellite Communications under Turbulence Effects, 2022 IEEE International Topical Meeting on Microwave Photonics (MWP), 2022, pp. 1–4.

Abstract: The optical signal propagation used in satellite uplinks and downlinks is influenced by absorption, scattering, and changes in the atmospheric refractive index or turbulence, causing optical signal attenuation. A free space optics (FSO) communications system using coherent communication can improve the link sensitivity and reach higher distances. This article proposes a new architecture for the phase detector in an all-digital optical phase-locked loop (OPLL) for coherent optical detection. Firstly, the performance of the proposed phase detector is evaluated under Gaussian noise, where the best operation point is found for the OPLL working with two sample rates: 625 MSa/s and 10 GSa/s. The system analyses also take a non-negligible delay into account. Then, it will be evaluated and compared with an OPLL using an analog phase detector in the presence of atmospheric turbulence. Finally, in three different atmospheric turbulence conditions, the effect of wind speed on communication quality is investigated through the obtained bit error rate (BER) from the recovered data for a bit rate of 20 Gbps. The results show that the proposed digital phase detector can track a signal under longer feedback loop delays and fading signals.

Keywords: atmospheric turbulence; coherent detection; optical digital phase-locked loop

Citation: Panasiewicz, J.; Arab, N.; Destic, F.; Pacheco, G.M.; Rissons, A. An All-Digital Optical Phase-Locked Loop Suitable for Satellite Downlinks. *Photonics* **2023**, *10*, 1312. <https://doi.org/10.3390/photonics10121312>

Received: 30 October 2023

Revised: 20 November 2023

Accepted: 25 November 2023

Published: 28 November 2023



Copyright: © 2023 by the authors. Licensee MDPI, Basel, Switzerland. This article is an open access article distributed under the terms and conditions of the Creative Commons Attribution (CC BY) license (<https://creativecommons.org/licenses/by/4.0/>).

1. Introduction

Due to the enormous increase in data traffic, multimedia service demands, and radio-frequency (RF) spectrum congestion, FSO has recently emerged as a promising communications technology [1]. As a result, switching to optical carriers has appeared as a solution to comply with the current and future demands. Furthermore, FSO has numerous advantages over RF communications, including large modulation bandwidth, narrow beam divergence, high security, high directivity, and no licensing requirement. However, optical signal propagation is impacted by absorption, scattering, and changes in the atmospheric refractive index or turbulence, which causes optical signal attenuation and degrades link quality [2].

Coherent optical communication is advantageous for long-distance FSO, such as satellite-to-ground links, as shown in Figure 1. It can achieve higher-order modulation formats, and better signal sensitivity [3]. Although coherent detection is widely used in fiber-optic networks, its use in satellite links is still in the research stage. For FSO communication, the two techniques used to recover the data in a coherent optical system are optical phase-locked loop (OPLL) and digital signal processing (DSP). OPLL is typically used in inter-satellite communication, while satellite-to-ground links can use adaptive optics (AO) in combination with DSP techniques [4].

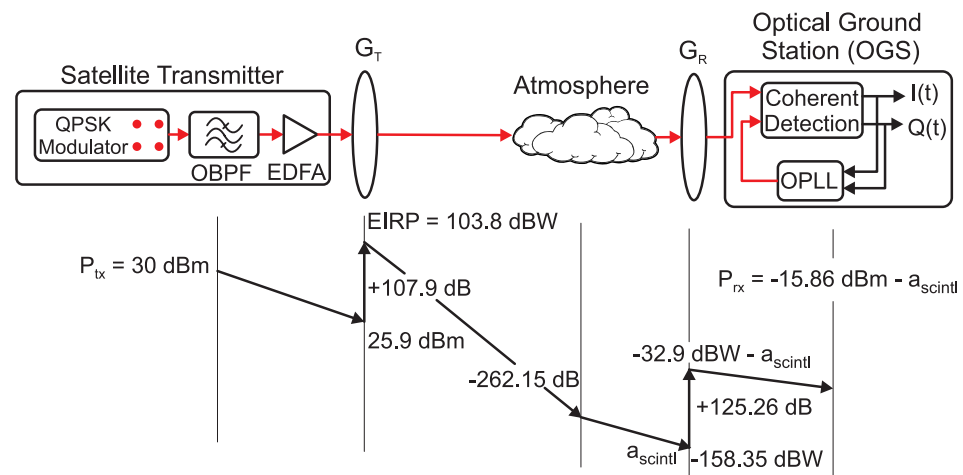


Figure 1. Power level diagram for the FSO downlink. G_T and G_R are the transmitter and receiver telescope gains, respectively, and EIRP stands for Effective Isotropic Radiated Power. The a_{scintl} is the attenuation caused by atmospheric turbulence.

For example, an FSO using BPSK modulation was demonstrated over a range of 10.45 km to emulate the atmospheric channel conditions for a geostationary feeder link and achieved a bit rate of 30 Gbps [5]. A digital synchronization system was evaluated inside a DSP, where a digital PLL and two open-loop techniques were analyzed [6]. Both systems were evaluated considering the effects of atmospheric turbulence and using the AO correction system.

Regarding the OPLL technique for FSO, an optical injection phase-locked loop (OIPLL) was demonstrated where a pilot carrier was transmitted to synchronize with the local oscillator [7]. The OIPLL was evaluated over the fiber optic transmission channel, and the atmospheric turbulence effects were not considered. For an inter-satellite link, an OPLL for a bit rate of 1 Gbps was demonstrated where a sensitivity of -59.2 dBm was achieved for a BER below 1×10^{-3} [8]. The analog OPLLs' structure is fixed to a specific modulation format due to the phase detector. Hence, the complexity of the OPLL phase detector increases with the modulation order. In addition, the loop time constants are fixed due to the components used, such as resistors and capacitors.

Therefore, the use of DSP and OPLLs appears in different scenarios and applications, each with advantages and disadvantages. As a result, using OPLL and DSP techniques such as real-time data recovery and parameter reconfiguration flexibility, a fully digital OPLL to demodulate a digitally modulated optical signal is proposed. In this way, an all-digital OPLL will be evaluated using the DSP technique for the phase detector to handle a fading signal. This signal results from the effects of atmospheric turbulence of an optical signal propagating a low Earth orbit (LEO) slant path shown in Figure 1. The system will be evaluated under three scenarios of atmospheric turbulence and several wind speed values, aided by simulations using VPIphotonics in a co-simulation technique. Hence, we extended our previous work, explaining the project decisions from OPLL behavior, the proposed hybrid approach, and the modification in the phase estimator used in DSPs [9]. Additionally, the OPLL is now analyzed using two sample rates: 625 MSa/s and 10 GSa/s.

2. Coherent Optical Receiver

2.1. LEO Slant Path

A general overview of the implemented system is shown in Figure 1. It shows a satellite downlink and its power level diagram considering the propagation of an optical signal digitally modulated with quadrature phase-shift keying (QPSK) and a bit rate of 20 Gbps. In addition, an optical band-pass filter (OBPF) filters the unwanted side lobes of the modulated optical signal, thereby reducing the transmitted bandwidth. The filtered optical signal is then amplified by an erbium-doped fiber amplifier (EDFA) to reach an

optical power of 30 dBm. Finally, the amplified pass through a telescope with a diameter $D_T = 12.5$ cm having a gain of approximately $G_T = 108$ dB and optics efficiency $\eta_T = 0.7$. Subsequently, the optical signal propagating through a slanted path of an LEO satellite, with a minimum elevation of 20° and an altitude of 700 km, is considered.

The transmitted optical signal is recovered in the optical ground station (OGS), where the telescope has a diameter of $D_R = 100$ cm, having a gain of approximately $G_R = 126$ dB, and an optics efficiency of $\eta_R = 0.65$. The received optical power after the propagation through the slant path, the telescope gains, and the transmission loss can be found in the link budget calculation [4,10,11]. Considering additional losses of 9 dB, such as coupling loss, the recovered optical signal has an optical power of approximately -16 dBm. The optical signal will be more attenuated according to the effects of the atmospheric turbulence a_{scint} , indicated in the power level diagram.

The OGS employs a coherent optical detector to retrieve the transmitted data. The coherent detector has a photodetector with a responsivity of $R = 0.04$ A/W, which gives a margin of 4 dB over the required input power. Consequently, the signal-to-noise ratio SNR can be determined by the following expression [12]:

$$\text{SNR} = \frac{RP_s}{qR_s} \tag{1}$$

where R is the photodetector responsivity, P_s is the received optical power, q is the electron charge (1.602×10^{-19} C), and R_s is the symbol rate. For QPSK modulation, the symbol-error rate (SER) is approximately denoted as [13]:

$$\text{SER} = \frac{1}{2} \text{erfc} \left(\sqrt{\frac{\text{SNR}}{2}} \right) \tag{2}$$

The above equation is approximately equal to the BER when the transmitted symbols are encoded with Gray code. Therefore, the modulation schemes used in this study will be encoded with the Gray code, where the above relations will be used to determine the theoretical BER curve.

2.2. Turbulence Model

The Earth’s atmosphere affects the performance of an optical communication link between an LEO satellite and an OGS. The three main processes that affect optical signal propagation are absorption, scattering, and fluctuations in the atmospheric refractive index or turbulence [2]. Absorption and scattering are caused by the molecules and particles that make up the atmosphere, which attenuates the optical signal. In the case of absorption, it occurs when a photon interacts with molecules in the atmosphere where it is absorbed.

Atmospheric turbulence is a phenomenon that originates in the thermodynamic exchanges between gases of different temperatures that compose the atmosphere. These thermodynamic exchanges generate movements of air masses, producing eddies of different refractive indices that move randomly, thus influencing the propagation of the optical signal. Due to the non-linear turbulence characteristics, the refractive index structure C_n^2 is the most important parameter in characterizing the effects of atmospheric turbulence. Furthermore, this refractive index depends on the geographical location, altitude, atmospheric conditions, and time of day. Due to these various dynamic parameters of the atmosphere, several models have been formulated to describe the C_n^2 profile. Among these models, the best known and most used in the literature is the Hufnagel–Valley model, whose profile is given by [2]:

$$C_n^2(h) = 8.148 \times 10^{-56} v_{rms}^2 h^{10} \exp^{-h/1000} + 2.7 \times 10^{-16} \exp^{-h/1500} + C_0 \exp^{-h/100} \text{ m}^{-2/3} \tag{3}$$

where h is the height above ground level (m), C_0 is the nominal value of C_n^2 at ground level ($\text{m}^{-2/3}$), and v_{rms} is the wind speed along the vertical path (m/s). In the simulations,

the nominal value of $C_n^2(0)$ at ground level will be considered with three different values of $1 \times 10^{-13} \text{ m}^{-2/3}$, $5 \times 10^{-14} \text{ m}^{-2/3}$, and $1 \times 10^{-15} \text{ m}^{-2/3}$, corresponding, respectively, to strong, moderate and weak turbulence. The International Telecommunication Union ITU-RP.1621-1 recommendation is used to calculate the corresponding ground wind speed through the Bufton wind model from the expression:

$$v_{rms} = \sqrt{v_g^2 + 33.11v_g + 360.31} \tag{4}$$

where v_g is the ground wind speed. The simulated wind speeds v_{rms} correspond to ground wind speeds ranging from zero to 43 m/s (zero to 154.8 km/h). By selecting this range of wind speeds, it is possible to simulate the optical link under various weather conditions (zero m/s during a calm summer day, 154 km/h during a storm). For different wind speed values, the $C_n^2(h)$ profile is modified only for an altitude between 5000 m and 20,000 m according to the Bufton model as shown in Figure 2. It's important to note that weak and strong turbulence exhibit the same behavior.

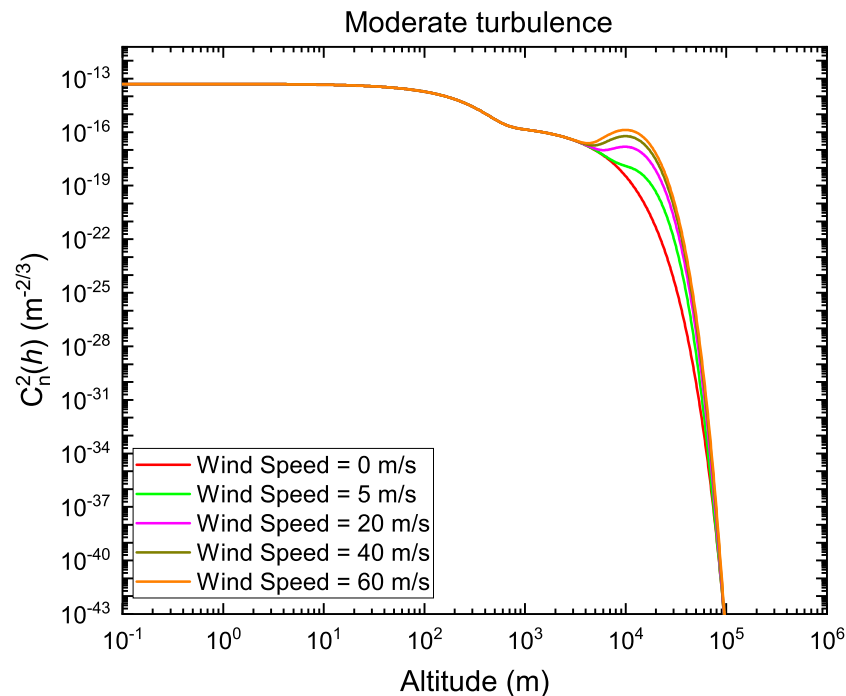


Figure 2. C_n^2 profile according to altitude for moderate turbulence and several wind speed values. The same behavior is obtained for weak and strong turbulence, changing only the $C_n^2(0)$ value.

The fluctuations in the refractive index in the atmosphere result in light scattering and variations in irradiance within the beam cross-section. Consequently, the optical wave will experience random power fading, resulting in a loss of signal-to-noise ratio. The scintillation index σ_I^2 defines the variations in the received optical power due to the scintillation. It is described as the normalized irradiance, or the received power, of the optical signal as:

$$\sigma_I^2 = \frac{\langle I^2 \rangle}{\langle I \rangle^2} - 1 = \frac{\langle I^2 \rangle - \langle I \rangle^2}{\langle I \rangle^2} \tag{5}$$

where $I \text{ (W/m}^2\text{)}$ denotes the irradiance of the optical signal. In other words, scintillation can cause power losses at the receiver and, eventually, fade the received signal, increasing the system's BER. Therefore, a mathematical description of the probability density function (PDF) of a randomly fading intensity signal can be used to determine the reliability of the FSO system in such an environment [2,14]. Therefore, several statistical models

for simulating the PDF of received power fluctuations have been proposed for different turbulent regimes.

This study will use the Log-Normal and Gamma-Gamma distributions among the various models to determine the PDF of the irradiance. The Log-Normal distribution model is valid only for weak and moderate turbulence regimes and is given by [2]:

$$p(I) = \frac{1}{I\sqrt{2\pi\sigma_I^2}} \exp \left[-\frac{\left(\ln\left(\frac{I}{I_0}\right) + \frac{1}{2}\sigma_I^2 \right)^2}{2\sigma_I^2} \right], \quad I > 0 \tag{6}$$

where I_0 is the irradiance in the absence of turbulence. For strong turbulent regimes, the Log-Normal PDF deviates from the experimental data. Thus, the Gamma-Gamma distribution is used for moderate to strong turbulence regimes. Therefore, the PDF of the optical signal scattered by the atmospheric turbulence can be represented as:

$$p(I) = \frac{2(\alpha\beta)^{(\alpha+\beta)/2}}{\Gamma(\alpha)\Gamma(\beta)} I^{(\alpha+\beta)/2-1} K_{\alpha-\beta}(2\sqrt{\alpha\beta}I), \quad (I > 0) \tag{7}$$

where K_b is the modified Bessel function of the second kind and order b . The α and β are the effective turbulence parameters related to the large-scale and small-scale scintillation of the optical wave. The expressions defining each parameter and their relation according to the FSO satellite link can be found in [2] (Chapter 12).

Thus, based on the previous definitions regarding scintillation, the modulated optical signal is calculated according to the realization of random fluctuations with PDF defined by the Gamma-Gamma function or Log-Normal distribution of the VPIphotonics turbulence model.

2.3. All-Digital OPLL Description

Figure 3 illustrates the block diagram of the implemented coherent optical receiver used in the OGS of Figure 1. In the coherent receiver, the trans-impedance amplifier (TIA) is used for loss compensation. In addition, a different approach is used to implement the local oscillator LO, known as an optical voltage-controlled oscillator (OVCO), for fine-tuning the optical signal [15]. It consists of a system formed by the laser, the dual-parallel Mach-Zehnder modulator (DPMZM), the 90° RF hybrid, and the electrical VCO. Due to the RF signals in quadrature, generating a single-side sub-carrier modulation is possible, thereby removing a stronger sub-carrier. The interface between a continuous-time system and a discrete-time is provided by an analog-to-digital converter (ADC), and the reverse conversion is performed by a digital-to-analog converter (DAC). The first-order active filter transfer function is a basis for the OPLL loop filter (LF). The combination with the VCO transfer function, an integrator, results in a second-order system. The LF transfer function is given by:

$$F(z) = K_1 + \frac{K_2}{1 - z^{-1}} \tag{8}$$

where K_1 , and K_2 are the loop filter gains, and z^{-1} is a symbol for a one-sample time delay in the z-domain. They can be found using the bilinear transformation, or Tustin's Rule, in the discrete-time system theory [16]. A signal-to-noise ratio (SNR) estimator was also implemented to determine noise variations on the demodulated signal and the OPLL. The second and fourth-order moments estimator, M2M4, is the basis of the SNR algorithm [17].

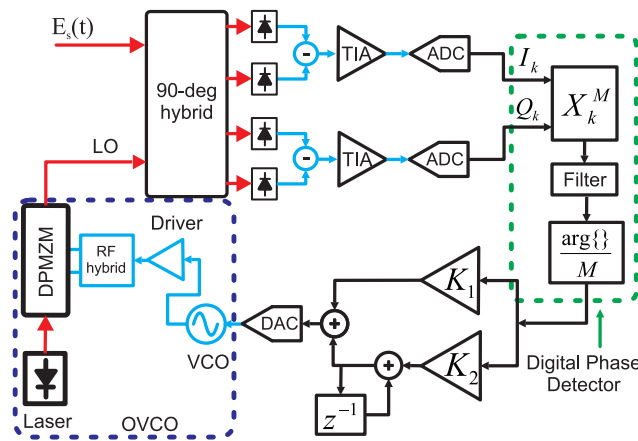


Figure 3. Block diagram of the implemented all-digital OPLL. The laser, the dual-parallel Mach-Zehnder modulator (DPMZM), the RF hybrid, and the VCO form an optical voltage-controlled oscillator (OVCO) shown inside the blue dashed block. The proposed digital discriminator is shown inside the green dashed block.

The phase detector’s block diagram is shown in Figure 3, inside the green dashed block. It provides information on phase error from a tracked carrier signal. However, as digital modulation suppresses the carrier, it has no carrier to be tracked. Therefore, based on the modulation scheme, a circuit removes the signal’s modulation, resulting in an unmodulated carrier to track when using an analog phase detector. For the modulation format used in this study, a circuit multiplied by four should be used to generate an error signal. The block diagram of this type of circuit used in QPSK modulation is shown in Figure 4.

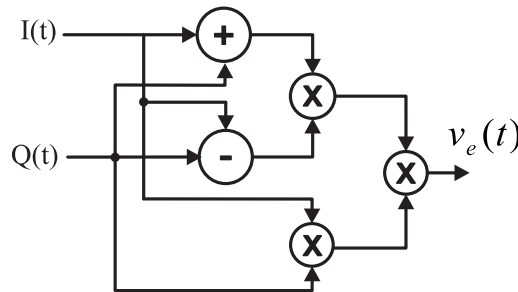


Figure 4. QPSK phase discriminator used in analog phase detector. The output error is proportional to $K_D \sin 4\theta$, where K_D is the phase detector gain and θ is the error signal [18].

The resulting error signal from the scheme shown in Figure 4 can be written as:

$$\begin{aligned}
 v_e(t) &= [(I(t)+Q(t)) \cdot (I(t) - Q(t))] \cdot (I(t) \cdot Q(t)) \\
 &= K_D \sin(4\theta_n(t)), \quad \text{where } K_D = \frac{G_{TIA}^4 R^4 P_s^2 P_{LO}^2}{4}
 \end{aligned}
 \tag{9}$$

where G_{TIA} is the trans-impedance gain, R is the responsivity, P_s is the modulated signal power, and P_{LO} is the power of the LO. These $I(t)$ and $Q(t)$ signals are the output of an optical coherent detector using a trans-impedance amplifier [18].

In the case of a discrete system, taking the imaginary part ($\Im m$) of the fourth power (QPSK) of the sample I/Q signals removes the modulation and recovers the phase-error signal. This operation results in the same gain as a circuit multiplication, where:

$$\Im m[X(k)^M] = \frac{\Im m[(I(k) + iQ(k))^M]}{M} = K_D \sin(M\theta)
 \tag{10}$$

where $X(k) = (I(k) + iQ(k))$ are the sampled I/Q signals written in a complex notation. For example, for QPSK, $M = 2^b = 4$, where M represents the modulation order, and b is the number of bits/symbols. This technique was proposed for a discrete-time decision-directed loop for OPLL synchronism [19]. Previously, an all-digital OPLL was demonstrated using a lookup table to implement the fourth power [20]. However, the projected control loop changes for a system subject to a fading signal since the gain K_D is related to the input signal level P_s . Consequently, the control loop behavior will change, making the OPLL unstable. Additionally, the phase error signal uses the approximation of $\sin(\theta) \approx \theta$, for small θ . Therefore, to use the phase error value without approximation, in this study, we propose a modification of a technique used in DSP systems. Figure 5a shows a block diagram for phase estimation used in the DSP technique. This method is based on the Viterbi–Viterbi algorithm, which is commonly used in DSPs for coherent optical systems [21,22].

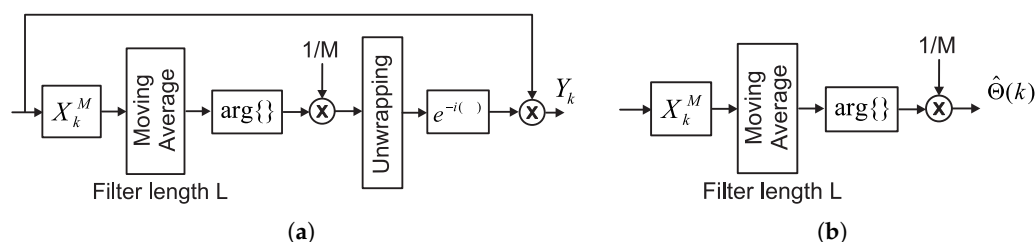


Figure 5. Block diagrams of phase estimation used in the DSP and the OPLL. (a) Block diagram of a phase compensation algorithm in DSP [18], (b) Block diagram of the proposed phase estimation process used in the OPLL.

Therefore, the input data $X(k)$ are complex multiplied by the estimated phase, where the resulting corrected signal will be $Y(k) = X(k) \cdot \exp[-i\hat{\Theta}(k)]$, where $\hat{\Theta}$ is the estimated phase. Thus, to obtain the estimated phase error value without approximation, a moving averaging filter (MAF) followed by the four-quadrant arc-tangent function is applied to the power moment of the sampled signals. Then, the estimated phase error can be expressed as:

$$\hat{\Theta}(k) = \frac{1}{M} \arg \left\{ \sum_{n=k+1}^{k+L} [X(n)]^M \right\} \tag{11}$$

In DSP, the described procedure is realized for blocks of data. However, this study is interested in carrier tracking, where the block diagram is modified and shown in Figure 5b. Thus, the estimated phase directly drives the loop filter input instead of having a multiplication for $\exp[-i\hat{\Theta}(k)]$. In this way, the phase is corrected sample by sample according to the sample rate of the digital PLL.

Regarding the MAF, the drawback of the power moment is the presence of harmonics at high frequencies in its output, which increases the OPLL phase error variance. For this reason, the MAF is employed to filter out the harmonics. Note that the MAF is a particular case of the finite impulse response (FIR) filter with all coefficients equal to $1/L$, where L is the average number of samples [23].

3. System Implementation and Analysis

3.1. OPLL

A co-simulation technique was used to develop and analyze the OPLL. The OPLL algorithm and SNR estimation were developed in Python, whereas the photonics circuit was implemented in VPIphotonics Design Suite. The parameters of the coherent detector are based on a commercial component with a responsivity of $R = 0.04$ A/W, and the G_{TIA} gain was set to 9 k Ω to achieve an eightfold increase in shot noise power over the thermal noise power for a P_{LO} of 1 dBm [24]. Furthermore, P_s changed as a result of the turbulence effects. The Tx and Rx lasers have a linewidth of 1 kHz for all analyses (based on the

availability of 1 kHz linewidth lasers—NKT Koheras BOOSTIK), and the VCO has a gain of 500 MHz/V with a center frequency of 20 GHz.

The propagation delay was also addressed, given that it may affect the OPLL, making it unstable. The MAF in the control loop represents a delay, where L taps introduce a delay of L samples. Furthermore, based on the commercial components, a delay of 12 ns was considered for the ADCs, and DAC [25]. For the *atan2*, based on the hardware implementation techniques, a delay of 15 ns was considered [26]. The OPLL sampling rate will consider two sample times to compare the behavior in the tracked signal. Firstly, the OPLL will be considered to work at a sample rate (SR) of 10 GSa/s motivated by the availability of ADCs, DACs, and even DSPs that can operate at 10 GHz, allowing the OPLL to collaborate with the DSP in a correction system. As the MAF will have 10 taps, it will introduce a delay of 1 ns.

The second scenario considers a relatively slow sample rate, or 625 MSa/s, where the key idea is to simulate an undersampling situation. In this case, the output data signal from the coherent detector is sampled with a frequency below the Nyquist criteria [27]. Consequently, the system could be operated with low sample rate ADCs and DACs. This scenario has already been demonstrated for OPLLs regarding optical communications [28] and free-space optical communication [20] where the atmospheric turbulence was not considered. Furthermore, the MAF will have five taps, thereby introducing a delay of 8 ns.

System simulations used an SR of 80 GSa/s, where the PLL working at the desired sample rate was implemented using the multi-rate sample processing technique [27]. For example, for 10 GSa/s, the SR is divided by eight by removing 8 bits from the sequence of bits. In the case of 625 MSa/s, the system follows the same procedure in which the SR is now divided by 128.

Traditionally, the LF parameters are determined by finding the optimal point through Norimatsu’s relation [29]. In this method, it is possible to find the optimal loop noise bandwidth for a determined feedback loop delay that will induce the lower power penalty for an analog LF implementation. According to this relation, by increasing the delay, the loop noise bandwidth should be increased to reduce the power penalty. Previous OPLLs used this method to find the optimal point, even using a digital approach to implement the LF where control system techniques such as lead-lag compensator were used to compensate the OPLL stability [8,20].

However, a digital approach is used to implement the LF where the loop noise bandwidth B_n must be specified relative to sample time T_s ($B_n T_s$ parameter where $B_n T_s \ll 1$). According to the Cramér-Rao bound limit, choosing small values of $B_n T_s$ improves the accuracy of the phase estimation [30]. Thus, for a fixed T_s value, the B_n should be increased to reduce the discriminator phase variance according to Norimatsu’s relation in case of a long feedback loop delay. However, it will increase the value of $B_n T_s$, which makes difficult the project of the OPLL since the parameter $B_n T_s$ should be reduced. Thus, the OPLL will be analyzed over several $B_n T_s$ values to find the phase-error variance and the induced penalty on the BER. The B_n will be changed to show the system behavior as the SR is fixed in two scenarios. The analyses will be conducted for the OPLL using the *atan2* discriminator since obtaining the variance and the standard deviation (STD) of the phase error directly from its output is possible.

The phase-error variance affects the BER by inducing a power penalty due to an imperfect carrier recovery. The probability of bit error due to the phase error for a QPSK modulation was previously calculated as [31]:

$$P_b(\sigma) = \frac{1}{2} \{ \operatorname{erfc} [\rho(\cos \sigma + \sin \sigma)] + \operatorname{erfc} [\rho(\cos \sigma - \sin \sigma)] \} \quad (12)$$

where $\rho = \sqrt{\frac{RP_s}{2R_s q}}$ and σ is the STD of the phase error. For example, the standard deviations of $\sigma = 3.1^\circ$ and $\sigma = 6^\circ$ correspond to power penalties of 0.5 dB and 1 dB at 1×10^{-9} BER, respectively. As a result, reducing the phase-error variance lowers the power penalty caused by the carrier synchronization error. In this sense, the analyses will start showing

the behavior of the OPLL system under several values of $B_n T_s$. Then, the power penalty induced for each condition will be shown for an SNR of 15.5 dB.

Figure 6 shows the discriminator output behavior under several values of $B_n T_s$ with an MAF of 10 coefficients. These conditions were simulated for an SNR of 15.5 dB at an SR of 10 Gsa/s, where each color represents one iteration, totaling 25 iterations. Figure 6a,b shows the output behavior for a B_n of 0.025 MHz and B_n of 1 MHz where the $B_n T_s = 2.5 \times 10^{-6}$ and $B_n T_s = 1 \times 10^{-4}$, respectively. Reducing the parameter $B_n T_s$ lowers the phase-error variance. However, the parameter $B_n T_s$ is reduced by lowering the B_n value, which lowers the ω_n (natural frequency) and slows the OPLL. As a result, it cannot correctly follow the laser variations, as shown in Figure 6a, which shows a fluctuation. This effect is even more pronounced using the SR of 625 MSa/s, which will be discussed next.

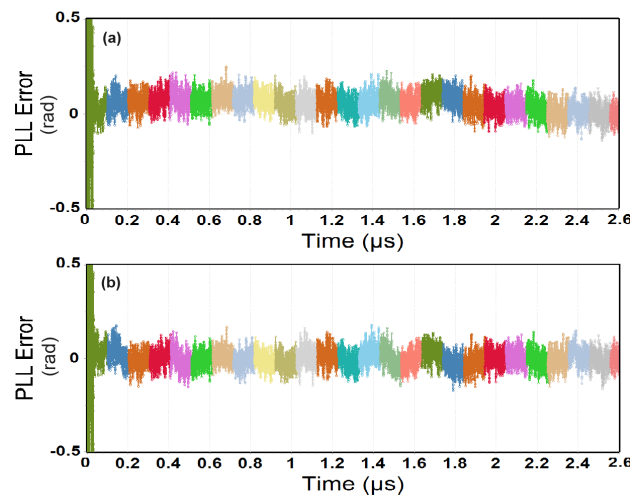


Figure 6. Discriminator output behavior under various $B_n T_s$ values with a sample rate of 10 Gsa/s and MAF with 10 coefficients. The laser linewidth was 2 kHz, and the feedback delay was 30 ns. (a) Output error for $B_n T_s = 2.5 \times 10^{-6}$, (b) Output error for $B_n T_s = 1 \times 10^{-4}$.

Figure 7 shows the discriminator output behavior with an MAF of five coefficients for various $B_n T_s$ values and an SNR of 15.5 dB. However, the SR is now 625 MSa/s, with each color representing one iteration as before. The output behavior for a B_n of 0.025 MHz, is shown in Figure 7 where $B_n T_s = 4 \times 10^{-5}$. Figure 7 depicts the output behavior for a B_n of 1 MHz, where $B_n T_s = 1.6 \times 10^{-3}$. The number of coefficients of the moving averaging filter also influences the phase variance, which will be discussed next.

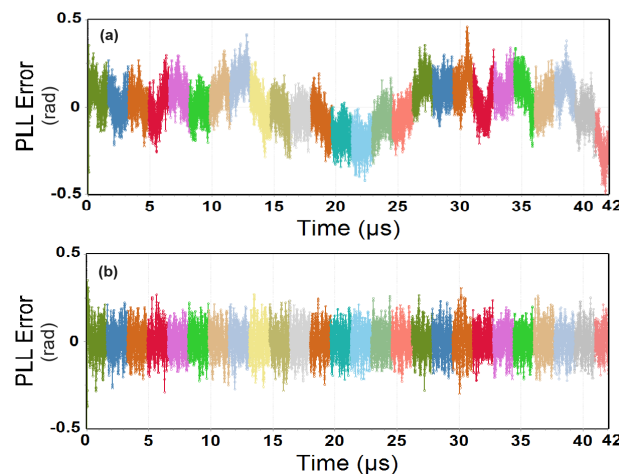


Figure 7. Discriminator output behavior under various $B_n T_s$ values with sample rate of 625 MSa/s and MAF with 5 coefficients. The laser linewidth was 2 kHz, and the feedback delay was 35 ns. (a) Output error for $B_n T_s = 4 \times 10^{-5}$, (b) Output error for $B_n T_s = 1.6 \times 10^{-3}$.

Despite using the same B_n value in both sampling rate scenarios, the OPLL is more impaired at a lower sampling rate. Comparing Figures 6a and 7a, one can see that the OPLL cannot correctly follow the signal variations since it has a fluctuation which in turn induces a fluctuation in the VCO center frequency. In this regard, the power penalty of different values of $B_n T_s$ was determined to find the smallest phase error, which consequently represents a lower degradation provided by the OPLL.

These analyses were carried out with an SNR of 15.5 dB, corresponding to a BER of 1×10^{-9} . Furthermore, eleven B_n values were considered, with each $B_n T_s$ value at both sampling rates analyzed using the MAF with 5 and 10 coefficients. For each value of $B_n T_s$, the OPLL was subjected to 25 iterations to obtain several samples of the standard deviation of the phase error. An average of these 25 standard deviation values was then calculated.

Figure 8a,b shows the standard deviation of the phase error for each $B_n T_s$ obtained for a sample rate of 10 GSa/s and 625 MSa/s, respectively. From these curves, it is possible to find a value of B_n that induces a desirable limit for the power penalty and keeps the OPLL with fast dynamics. For example, Figure 8b shows a minimum for the phase error at $B_n T_s = 0.8 \times 10^{-3}$ ($B_n = 0.5$ MHz), which will induce a lower penalty. In Figure 8a, on the other hand, the phase error is practically flat in all analyzed B_n values, where the power penalty is almost the same. Therefore, these analyses show that low sample rates will induce a higher power penalty than high SRs.

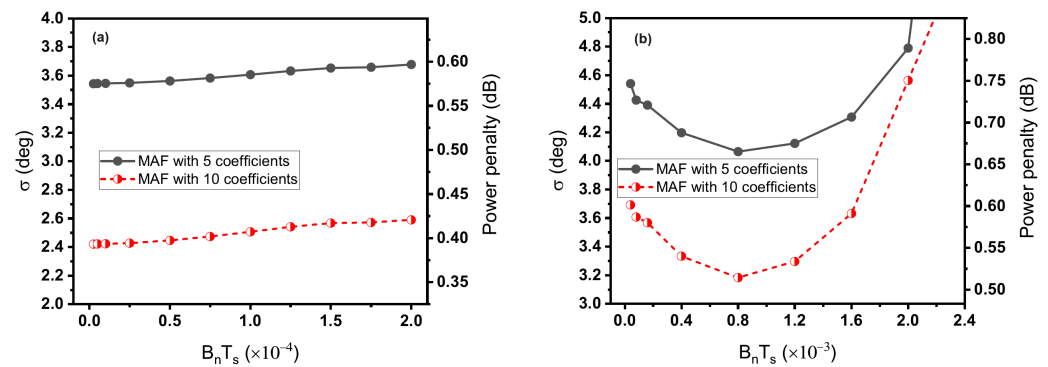


Figure 8. OPLL phase error and the induced power penalty for several $B_n T_s$ at both sample rates and MAF coefficients number. (a) Phase error and power penalty for several $B_n T_s$ values at 10 GSa/s, (b) Phase error and power penalty for several $B_n T_s$ values at 625 MSa/s.

Another observation from these analyses is the influence of the number of MAF coefficients. Increasing the number of coefficients reduces the variance of the phase error, and consequently, the power penalty caused by the OPLL. However, as discussed earlier, increasing the number of coefficients increases the system delay. Thus, a trade-off must be chosen between the number of MAF coefficients and the feedback delay. For example, if a power penalty of 0.67 dB is allowed at 625 MSa/s, the number of MAF coefficients can be increased, which allows the feedback delay to increase. However, the additional delay can make the OPLL unstable since it reduces the projected phase margin, which should be compensated using a lead-lag compensator, for example.

Finally, from these analyses, the OPLL was defined to work with a $B_n = 2$ MHz for an SR of 10 GSa/s ($B_n T_s = 2 \times 10^{-4}$), with a power penalty of 0.42 dB found for a standard deviation of 2.6° . For an SR of 625 MSa/s, the OPLL was defined to work with a $B_n = 500$ kHz ($B_n T_s = 0.8 \times 10^{-3}$), where a power penalty of 0.66 dB was found for a standard deviation of 4.06° .

3.2. Results

The previously performed analyses lay the groundwork for the turbulence analyses conducted in this section. The OPLL was evaluated through variations of the turbulence

channel where the two proposed SRs were evaluated. The proposed digital discriminator was also compared with the imaginary part of the fourth-power moment for each SR.

In an OPLL, the phase error variance will reflect on the phase noise of the controlled frequency. Thus, one measure of comparison would be to compare the variances of the two discriminators. However, since they have different gains, the variance calculation is impaired. Therefore, the STD of the controlled frequency will be used as a metric for comparing the performance of the two discriminators.

Figure 9 shows the VCO output frequency behavior for a strong turbulence regime and a wind speed of 60 m/s for the OPLL working with an SR of 10 GSa/s. Figure 10 shows the VCO output frequency behavior for the same atmospheric turbulence conditions, however for the OPLL working with an SR of 625 MSa/s. Each color represents the fade values where the system is analyzed for thirty different values or thirty iterations. These values were the random fluctuations determined by the turbulence model, resulting in the estimated SNR level shown in Figure 11.

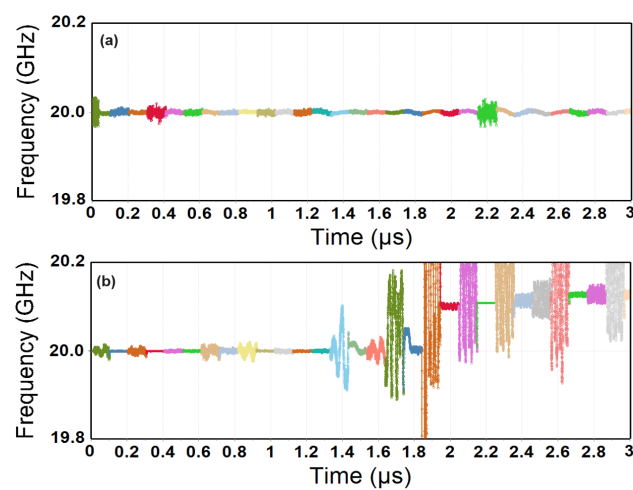


Figure 9. VCO output frequency behavior under strong turbulence and wind speed of 60 m/s for the OPLL working with SR of 10 GSa/s. (a) OPLL using the proposed digital phase detector, (b) OPLL using the sinusoidal discriminator.

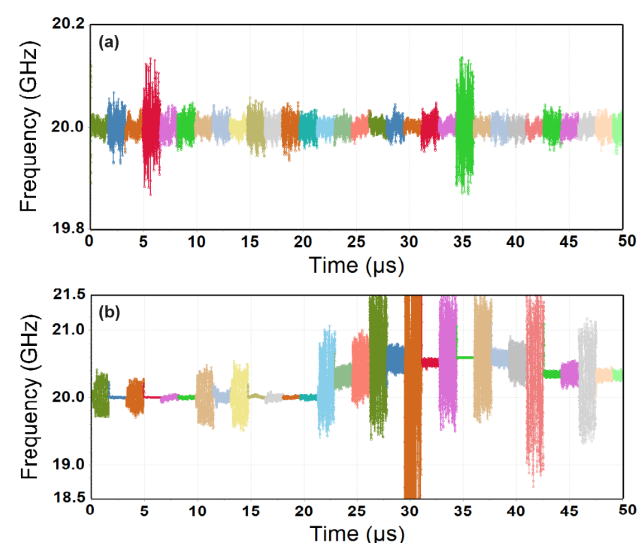


Figure 10. VCO output frequency behavior under strong turbulence and wind speed of 60 m/s for the OPLL working with SR of 625 MSa/s. (a) OPLL using the proposed digital phase detector, (b) OPLL using the sinusoidal discriminator.

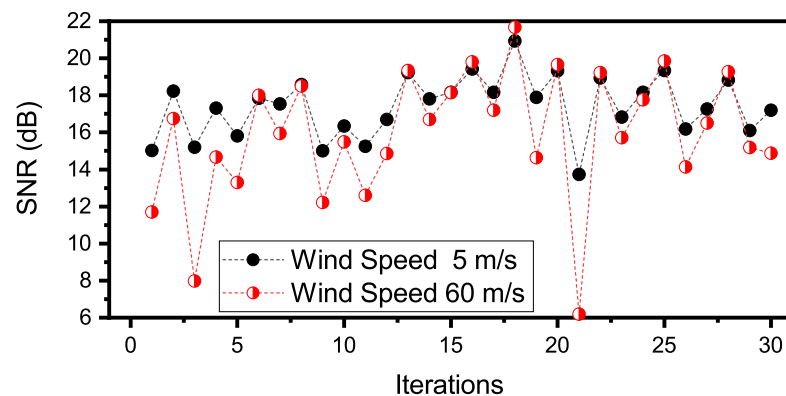


Figure 11. SNR level variations for wind speeds of 5 m/s and 60 m/s under strong turbulence. Each point represents a turbulence event totaling thirty different values or thirty iterations.

The VCO output frequency behavior using the digital discriminator (*atan2*) and the imaginary part (*sine*) is shown in Figures 9a and 9b, respectively, for an SR of 10 GSa/s. For an SR of 625 MSa/s, the VCO output frequency behavior is shown in Figure 10a,b. For an SR of 10 GSa/s, the OPLL with the *atan2* discriminator was studied with a total delay of 30 ns, whereas the *sine* phase detector was analyzed with a total delay of 6 ns, as it became unstable with delays longer than that. For an SR of 625 MSa/s, as the B_n value decreased, both discriminators were analyzed under a total delay of 35 ns. The MAF has five taps, representing a delay of 8 ns. The *sine* discriminator presents a higher oscillatory characteristic and an STD of the controlled frequency. The STD variation is related to the gain of the *sine* discriminator since its gain, as shown previously, depends on the system parameters. As the input power level changes due to turbulence, the gain also changes, reflecting the OPLL phase error variance and the controlled frequency STD. Also, as indicated by the variation of the central frequency, the OPLL loses the lock during higher fading and cannot recover the track signal.

For all turbulence scenarios, the proposed digital discriminator had the same gain of 1 in both SRs. As the phase error is computed using the *I/Q* signals, the *atan2* has the advantage of being independent of system parameters. As a result, without modifying the OPLL project, it was possible to analyze the system under various turbulence scenarios. It also has a low STD of the controlled frequency, as shown in Figures 9a and 10a. For example, comparing the STD of both SRs for an SNR of approximately 8 dB (third event in Figure 11), the OPLL at 10 GSa/s shows an STD of ± 6.5 kHz while the OPLL at 625 MSa/s shows an STD of ± 34 kHz. This is due to its higher phase error variance, as previously discussed. The ability of the *atan2* discriminator to track the signal despite longer feedback loop delays and fading is one of its most notable characteristics. Hence, the *atan2* provides an alternative to digital OPLL due to its performance in the presence of noise and its tracking capability. In both SRs, the *atan2* and *sine* discriminators were also compared in other wind speed values and turbulence scenarios. While the proposed discriminator maintains the system locked, the sinusoidal discriminator always loses the lock during the fading regime. The sinusoidal discriminator only maintained locking when the system delay was equal to zero, which was an unrealistic condition.

The effect of wind speed on system performance was also investigated in both SRs due to the proposed phase detector's tracking capability under fading regimes. Thus, the BER fluctuation according to wind speed in three different turbulent conditions (weak, moderate, and strong) is shown in Figure 12. The OPLL at an SR of 625 MSa/s shows a higher degradation compared to the OPLL at 10 GSa/s, as it exhibits a higher power penalty, as previously discussed. In Figure 12, each point represents the average BER calculated for thirty different events. Therefore, by simulating only thirty events, it was evaluated that the results were representative. As a result, the error caused by the number

of simulated events may be negligible, where it was chosen as a compromise between results and simulation time.

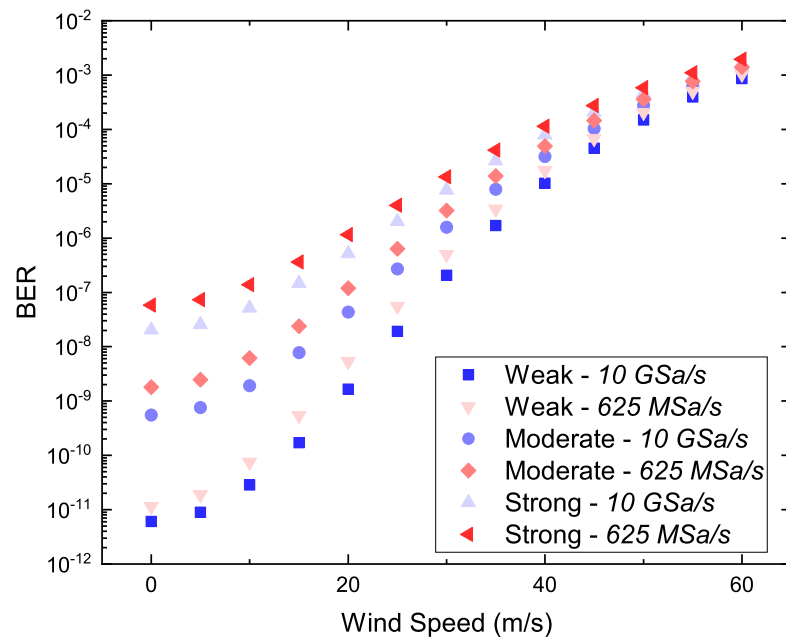


Figure 12. BER variation (mean of 30 events) as a function of wind speed for the OPLL using the digital discriminator and working with an SR of 625 MSa/s and 10 GSa/s. The OPLL at an SR of 625 MSa/s shows a higher degradation due to its higher power penalty.

Regarding the wind speed impact on the optical signal, the turbulence intensity contributes to data degradation for wind speeds lower than 20 m/s. However, for v_{rms} higher than that, it influences the degradation of the transmitted data more than the turbulence’s intensity. Hence, when the wind speed is 60 m/s, as shown in Figure 12, the BER is influenced mainly by the wind speed for all the turbulence scenarios, thereby degrading the transmitted data.

4. Discussion

In this study, we have presented the evaluation of the OPLL using two sample rates to compare the behavior of *sine* and *atan2* phase discriminators. The *atan2* showed a superior performance regarding the standard deviation of the controlled frequency. The moving average filter helps eliminate the harmonics of the power moment, decreasing the phase-error variance. Consequently, the low STD results from a better phase estimation and a low phase variance since the *atan2* output is the phase error.

Another motivation for using the *atan2* is a scenario under low SNR conditions. If only the imaginary part of Equation (10) is used as a phase detector, it is susceptible to amplitude variations, as shown in the simulations. Thus, the OPLL loses lock under low SNR conditions or presents a significant error. An automatic gain control circuit must be employed to compensate for these amplitude variations. Using the four-quadrant arctangent discriminator improves the sensitivity of the PLL since its error output is a relation between the I and Q signals.

Table 1 compares previously reported optical coherent receivers using the DSP or the OPLL for signal recovery with this study’s proposed method. As shown in Table 1, previous studies used the Viterbi–Viterbi (VV) algorithm in data blocks for phase estimation in the case of DSPs or an analog phase detector or exclusive or gate (XOR) for the OPLL. In contrast to previous techniques, our proposed system uses a hybrid approach where the OPLL works as a complement in a DSP correction system. Thus, the Viterbi–Viterbi algorithm is applied synchronously according to the system SR.

Table 1. Comparison of previous optical coherent receivers.

| | [5,18,21,22] | [7,8,20,32] | This Study |
|------------------|--------------------------|--|------------------------------------|
| Methods | DSP | OPLL or OIPLL | Hybrid DSP-OPLL |
| Phase estimation | VV algorithm data blocks | XOR gate, analog multiplier, or fourth-power look-up table | VV algorithm synchronously with SR |

Furthermore, the advent of integrated photonics [33] and higher sample rate systems would make integrating both systems (OPLL and DSP) possible. For example, the VCO could be replaced by a direct digital synthesizer (DDS) that would digitally generate the microwave carrier. An OPLL employing DDS in place of VCO was previously reported [20].

Due to its performance, the *atan2* discriminator was evaluated under scenarios of atmospheric turbulence. Both discriminators were compared in three scenarios: weak, moderate, and strong turbulence. These turbulence regimes induce power fading levels on the transmitted optical signal, affecting the OPLL tracking capability. The fading effect was very pronounced on the *sine* discriminator since its gain depends on the signal level. Since the output of the *atan2* discriminator is independent of the signal level input, its performance is transparent under scintillation fading effects. Consequently, the OPLL keeps tracking the input signal in different turbulence regimes.

Regarding the atmospheric turbulence, in the model, the independent scintillation events occur on a timescale of μs to ms . Consequently, the turbulence applies independent scintillations to the OPLL, corresponding to one iteration. As a result, even though the simulation only lasts a few microseconds, every iteration represents a scintillation event. Consequently, the model illustrates an abrupt change in the SNR level of the optical signal when it passes between several scintillation events. Regardless of the decreased SNR level, the OPLL utilizing the proposed digital discriminator remains locked due to its characteristics, as previously discussed.

5. Conclusions

A new architecture for the phase detector was presented for an all-digital OPLL to demodulate a digitally modulated optical signal. The phase discriminator is a digital type that can track a signal under longer feedback loop delays and fading signals. It was based on modifying the traditional algorithm used in coherent optical communications. This phase detector made it possible to find the best operation point for the OPLL, which was then used to handle the effects of atmospheric turbulence. In addition, the OPLL using the digital discriminator showed a low standard deviation of the controlled frequency and low phase noise, making it an alternative for fully digital OPLLs.

Moreover, the OPLL was analyzed working with two sample rates, showing that low sample rates will have a higher phase error variance, and consequently, a higher power penalty. Furthermore, due to the phase discriminator features, the OPLL could be analyzed in different scenarios of atmospheric turbulence and wind speed values. It was observed that traditional analog detectors, which have a sinusoidal characteristic, are unsuitable for a system that fluctuates the input signal amplitude. This is due to the analog detector gain related to the system parameters, such as the input signal amplitude.

It also has been observed that the system degrades when increasing the wind speed and turbulence. However, wind speed is the principal cause of system degradation for speeds higher than 20 m/s. During the simulations, the scintillation index behavior was observed to be comparable to the obtained BER profiles. The hardware implementation of the OPLL using the proposed digital discriminator is currently being developed.

Author Contributions: Conceptualization, J.P.; methodology, J.P. and N.A.; software, J.P.; validation, J.P., N.A. and F.D.; formal analysis, J.P.; investigation, J.P. and N.A.; resources, F.D. and A.R.; data curation, J.P. and N.A.; writing—original draft preparation, J.P.; writing—review and editing, J.P., N.A., F.D., G.M.P. and A.R.; supervision, G.M.P. and A.R.; funding acquisition, J.P. All authors have read and agreed to the published version of the manuscript.

Funding: This work was supported by Conselho Nacional de Desenvolvimento Científico e Tecnológico (CNPq/Brazil) under Grant 201259/2018-4.

Institutional Review Board Statement: Not applicable.

Informed Consent Statement: Not applicable.

Data Availability Statement: The dataset generated during the current study are available from the corresponding author upon reasonable request.

Conflicts of Interest: The authors declare no conflict of interest.

References

1. Kaushal, H.; Kaddoum, G. Optical Communication in Space: Challenges and Mitigation Techniques. *IEEE Commun. Surv. Tutor.* **2017**, *19*, 57–96. [[CrossRef](#)]
2. Andrews, L.C.; Phillips, R.L. *Laser Beam Propagation through Random Media*, 2nd ed.; SPIE Press: Bellingham, WA, USA, 2005.
3. Winzer, P.J.; Neilson, D.T.; Chraplyvy, A.R. Fiber-optic transmission and networking: The previous 20 and the next 20 years. *Opt. Express* **2018**, *26*, 24190–24239. [[CrossRef](#)] [[PubMed](#)]
4. Carrasco-Casado, A.; Mata-Calvo, R. Space Optical Links for Communication Networks. In *Springer Handbook of Optical Networks*; Mukherjee, B., Tomkos, I., Tornatore, M., Winzer, P., Zhao, Y., Eds.; Springer Handbooks; Springer International Publishing: Cham, Switzerland, 2020; pp. 1057–1103. [[CrossRef](#)]
5. Surof, J.; Poliak, J.; Calvo, R.M. Demonstration of Intradyne BPSK Optical Free-Space Transmission in Representative Atmospheric Turbulence Conditions for Geostationary Uplink Channel. *Opt. Lett.* **2017**, *42*, 2173. [[CrossRef](#)] [[PubMed](#)]
6. Paillier, L. Architecture de Récepteur Cohérent Pour les Liens Optiques Satellite-Sol Avec Optique Adaptative. Ph.D. Thesis, Institut Polytechnique de Paris, Palaiseau, France, 2020.
7. Shoji, Y.; Fice, M.J.; Takayama, Y.; Seeds, A.J. A Pilot-Carrier Coherent LEO-to-Ground Downlink System Using an Optical Injection Phase Lock Loop (OIPLL) Technique. *J. Light. Technol.* **2012**, *30*, 2696–2706. [[CrossRef](#)]
8. Yue, C.; Li, J.; Sun, J.; Zhu, R.; Hou, X.; Zhang, X.; Liu, L.; Chen, W. Homodyne Coherent Optical Receiver for Intersatellite Communication. *Appl. Opt.* **2018**, *57*, 7915–7923. [[CrossRef](#)] [[PubMed](#)]
9. Panasiewicz, J.; Arab, N.; Destic, F.; Pacheco, G.M.; Rissons, A. All-Digital Optical Phase-Locked Loop for satellite communications under Turbulence Effects. In Proceedings of the 2022 IEEE International Topical Meeting on Microwave Photonics (MWP), Orlando, FL, USA, 3–7 October 2022; IEEE: Piscataway, NJ, USA, 2022; pp. 1–4.
10. Kaushal, H.; Jain, V.; Kar, S. *Free Space Optical Communication*; Optical Networks; Springer: New Delhi, India, 2017. [[CrossRef](#)]
11. Gigenbach, D.; Knopp, M.T.; Fuchs, C. Link budget calculation in optical LEO satellite downlinks with on/off-keying and large signal divergence: A simplified methodology. *Int. J. Satell. Commun. Netw.* **2023**, *41*, 460–476. [[CrossRef](#)]
12. Ho, K.P. *Phase-Modulated Optical Communication Systems*; Springer Science & Business Media: Berlin, Germany, 2005.
13. Kikuchi, K. Fundamentals of Coherent Optical Fiber Communications. *J. Light. Technol.* **2016**, *34*, 157–179. [[CrossRef](#)]
14. Majumdar, A.K. *Advanced Free Space Optics (FSO): A Systems Approach*; Springer Series in Optical Sciences; Springer: New York, NY, USA, 2015; Volume 186. [[CrossRef](#)]
15. Ferrero, V.; Camatel, S. Optical Phase Locking Techniques: An Overview and a Novel Method Based on Single Side Sub-Carrier Modulation. *Opt. Express* **2008**, *16*, 818. [[CrossRef](#)] [[PubMed](#)]
16. Rice, M. *Digital Communications: A Discrete-Time Approach*; Pearson Prentice Hall: Hoboken, NJ, USA, 2009.
17. Pauluzzi, D.R.; Beaulieu, N.C. A Comparison of SNR Estimation Techniques for the AWGN Channel. *IEEE Trans. Commun.* **2000**, *48*, 1681–1691. [[CrossRef](#)]
18. Schaefer, S.; Gregory, M.; Rosenkranz, W. Coherent Receiver Design Based on Digital Signal Processing in Optical High-Speed Intersatellite Links with M-Phase-Shift Keying. *Opt. Eng.* **2016**, *55*, 111614. [[CrossRef](#)]
19. Barry, J.R.; Kahn, J.M. Carrier Synchronization for Homodyne and Heterodyne Detection of Optical Quadrature-Shift Keying. *J. Light. Technol.* **1992**, *10*, 1939–1951. [[CrossRef](#)]
20. Lu, S.; Zhou, Y.; Zhu, F.; Sun, J.; Yang, Y.; Zhu, R.; Hu, S.; Zhang, X.; Zhu, X.; Hou, X.; et al. Digital-Analog Hybrid Optical Phase-Lock Loop for Optical Quadrature Phase-Shift Keying. *Chin. Opt. Lett.* **2020**, *18*, 090602. [[CrossRef](#)]
21. Tsukamoto, S.; Katoh, K.; Kikuchi, K. Coherent Demodulation of Optical Multilevel Phase-Shift-Keying Signals Using Homodyne Detection and Digital Signal Processing. *IEEE Photonics Technol. Lett.* **2006**, *18*, 1131–1133. [[CrossRef](#)]
22. Kikuchi, K. Phase-diversity homodyne detection of multilevel optical modulation with digital carrier phase estimation. *IEEE J. Sel. Top. Quantum Electron.* **2006**, *12*, 563–570. [[CrossRef](#)]

23. Collins, T.F.; Getz, R.; Pu, D.; Wyglinski, A.M. *Software-Defined Radio for Engineers*; Mobile Communications Series; Artech House Publishers: Boston, MA, USA; London, UK, 2018.
24. Herzog, F.T. An Optical Phase Locked Loop for Coherent Space Communications. Ph.D. Thesis, ETH Zurich, Zurich, Switzerland, 2006. [[CrossRef](#)]
25. Chen, X.; Liu, X.; Zhang, Y.; Shan, Y.; Hu, Q.; Li, J.; Lan, S. Z-Domain Modeling Methodology for Homodyne Digital Optical Phase-Locked Loop. *IEICE Electron. Express* **2021**, *18*, 20210078. [[CrossRef](#)]
26. De Dinechin, F.; Istoan, M. Hardware Implementations of Fixed-Point Atan2. In Proceedings of the 2015 IEEE 22nd Symposium on Computer Arithmetic, Lyon, France, 22–24 June 2015; pp. 34–41. [[CrossRef](#)]
27. Oppenheim, A.V.; Buck, J.R.; Schafer, R.W. *Discrete-Time Signal Processing*, 2nd ed.; Prentice Hall: Upper Saddle River, NJ, USA, 1999.
28. Sakamoto, T.; Lu, G.W.; Chiba, A.; Kawanishi, T. Digital Optical Phase Locked Loop for Real-Time Coherent Demodulation of Multilevel PSK/QAM. In Proceedings of the 2010 Conference on Optical Fiber Communication (OFC/NFOEC), Collocated National Fiber Optic Engineers Conference, San Diego, CA, USA, 21–25 March 2010; pp. 1–3. [[CrossRef](#)]
29. Norimatsu, S.; Iwashita, K. PLL Propagation Delay-Time Influence on Linewidth Requirements of Optical PSK Homodyne Detection. *J. Light. Technol.* **1991**, *9*, 1367–1375. [[CrossRef](#)]
30. Hamkins, J.; Simon, M.K. Carrier Synchronization. In *Autonomous Software-Defined Radio Receivers for Deep Space Applications*; Jet Propulsion Laboratory, California Institute of Technology: Pasadena, CA, USA, 2006; p. 227.
31. Rhodes, S. Effect of Noisy Phase Reference on Coherent Detection of Offset-QPSK Signals. *IEEE Trans. Commun.* **1974**, *22*, 1046–1055. [[CrossRef](#)]
32. Liu, Y.; Zhao, X.; Tong, S.; Chang, S.; Song, Y.; Dong, Y.; An, Z.; Yu, F. Study of Multistage Composite Loop Control Based on Optical Phase-Locked Loop Technology. *Opt. Commun.* **2018**, *424*, 17–25. [[CrossRef](#)]
33. Lu, M.; Park, H.c.; Bloch, E.; Sivananthan, A.; Parker, J.S.; Griffith, Z.; Johansson, L.A.; Rodwell, M.J.W.; Coldren, L.A. An Integrated 40 Gbit/s Optical Costas Receiver. *J. Light. Technol.* **2013**, *31*, 2244–2253. [[CrossRef](#)]

Disclaimer/Publisher’s Note: The statements, opinions and data contained in all publications are solely those of the individual author(s) and contributor(s) and not of MDPI and/or the editor(s). MDPI and/or the editor(s) disclaim responsibility for any injury to people or property resulting from any ideas, methods, instructions or products referred to in the content.